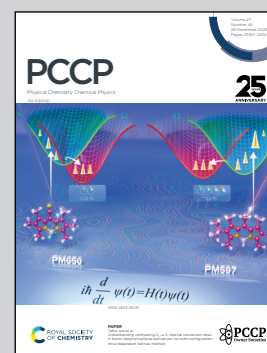**Showcasing work from the group of Dr Tobias Dickbreder**

Nanoscopic feldspar islands on K-feldspar microcline (001)

This study investigates the atomic structure of the (001) cleavage plane of natural microcline samples in ultrahigh vacuum and at the solid–liquid interface. Samples were found to exhibit nanometre-sized islands with the same atomic structure as the microcline terraces suggesting that these islands are an intrinsic surface feature. Further, the islands are stable in contact with water indicating that the island structure might persist under environmental conditions. Since these islands significantly increase the number of edge and kink sites on the surface, they are expected to have important implications for surface reactivity and processes.

Image reproduced by permission of Tobias Dickbreder from *Phys. Chem. Chem. Phys.*, 2025, **27**, 23574.

As featured in:

See Tobias Dickbreder *et al.*, *Phys. Chem. Chem. Phys.*, 2025, **27**, 23574.

ROYAL SOCIETY
OF **CHEMISTRY**

rsc.li/pccp

Registered charity number: 207890

PCCP
Owner Societies

Check for updates

Nanoscopic feldspar islands on K-feldspar microcline (001)†

Tobias Dickbreder, ★[ab] Franziska Sabath, ‡[a] Florian Schneider, [a] Uwe Güth,[c] Ralf Bechstein[a] and Angelika Kühnle[a]

Feldspar minerals are abundant rock-forming minerals playing a central role in environmental processes such as silicate weathering and ice nucleation in mixed-phase clouds. These processes typically take place at the feldspar–water interface, which is why the micro- and nanoscopic surface topology is of major importance to understand them. However, especially in the field of ice nucleation on feldspar surfaces, most experimental studies are limited to the micrometre scale, while the ice nucleation sites are expected to be nanometre sized. Here, we report an intrinsic island structure observed on microcline (001). High-resolution atomic force microscopy (AFM) images taken in ultra-high vacuum show nanometre-sized islands on the terraces and at the step edges. Atomic scale images revealing a very similar contrast and identical lattice parameters on the terrace and on the islands suggest that these islands are an intrinsic feature of the microcline surface. Moreover, AFM at the solid–liquid interface demonstrates that the observed nanostructure is stable in water. As the existence of islands significantly increases the density of edge and kink sites, the observed nanostructure might have important implications for surface reactivity and potentially ice nucleation efficiency.

1 Introduction

Due to their wide abundance, feldspar minerals play a central role in many large scale environmental processes. In the lithosphere, feldspar minerals are not only major constituents of most igneous rocks, they are also abundant in metamorphic and sedimentary rocks.[1] Weathering of these rocks ultimately leads to the formation of carbonate minerals, binding atmospheric carbon in the process. This process, referred to as the carbonate–silicate cycle, is of utmost importance for life on Earth, as one of the major temperature feedbacks regulating our climate *via* the atmospheric carbon dioxide level.[2] Based on this natural process, artificial silicate weathering has also been discussed as a means to capture anthropogenic carbon dioxide.[3,4] Moreover, erosion can create small feldspar

particles, which are then picked up by the wind and brought into the atmosphere.[5] Airborne feldspar particles, especially alkali feldspar, are very efficient ice nucleating particles under mixed-phase cloud conditions.[6–8] That is, they initiate the formation of ice in clouds in a temperature range where cloud droplets would normally stay liquid due to kinetic hindrance. This change in aggregate state has a profound impact on the physical and chemical properties of clouds such as their lifetime and reflectivity,[5,9,10] making a detailed understanding of this process necessary for the development of accurate climate models.[11]

Both, weathering and heterogeneous ice nucleation, typically take place at the interface between feldspar minerals and aqueous solution. Hence, a detailed understanding of the feldspar–water interface is essential for unravelling these large-scale processes. Understanding the feldspar–water interface requires a careful consideration of the complex interplay between interfacial chemistry and surface topology. The former refers to the species present at the interface, their chemical environment and reactivity, and the latter refers to placement and abundance of surface features such as terraces, step edges, and kink sites. While, at first glance, the surface chemistry may seem as the primary impact factor for the interfacial reactivity, it is important to acknowledge the effect of surface topology. Many interfacial processes such as dissolution and growth of minerals predominantly take place at edge and kink sites and not on the flat terrace.[12–14] Consequently, the presence

[a] *Physical Chemistry I, Faculty of Chemistry, Bielefeld University, Universitätstraße 25, 33615 Bielefeld, Germany*

[b] *University of Vienna, Faculty of Chemistry, Institute of Physical Chemistry, Währinger Straße 42, 1090 Vienna, Austria.*
E-mail: tobias.dickbreder@univie.ac.at

[c] *Physical Chemistry III, Faculty of Chemistry, Bielefeld University, Universitätstraße 25, 33615 Bielefeld, Germany*

† Electronic supplementary information (ESI) available: All recorded channels of overview images, AFM image showing atomic resolution on both terrace and islands and annealing experiments. AFM raw data files in Gwyddion Native format (gwy). See DOI: https://doi.org/10.1039/d5cp00610d

‡ Present address: Max Planck Institute for Polymer Research, 55128 Mainz, Germany.

23574 | *Phys. Chem. Chem. Phys.*, 2025, **27**, 23574–23583

This journal is © the Owner Societies 2025

(or absence) of such surface features can have an enormous impact on the reactivity of minerals.

For feldspar minerals, the role of microtexture in the bulk and surface structure has been studied extensively for a long time.[15,16] Alkali feldspars (chemical formula $XAlSi_3O_8$ with X = Na, K) form a continuous mixing series at the elevated temperatures present during the formation of most feldspar minerals, but not at room temperature.[1,17] Hence, the initially-formed homogeneously mixed alkali feldspars exsolve into Na- and K-rich domains during cooling or in the course of their geological history.[1] The combination of exsolution processes with weathering gives rise to a wide range of complex so-called perthitic intergrowth in the bulk and on the surface of alkali feldspar minerals.[1,15] Typical forms of perthitic intergrowth described in literature are lamellae,[18–21] platelets[22,23] and nanotunnels.[18,24] Moreover, patch and vein morphologies have been observed.[25,26]

In addition to studies discussing feldspar microtexture in the general geological context, the microtexture of alkali feldspar has also attracted great interest in light of ice nucleation activity. Several independent studies show that ice nucleation on alkali feldspar minerals does not start on flat areas but at distinct surface features such as cracks or pores.[27–33] This seems to hold true for ice nucleation in both immersion and deposition mode, even though the active sites on alkali feldspar differ between modes.[29] In deposition mode, environmental scanning electron microscopy reveals the same preferential orientation on the (001) and (010) surfaces of microcline feldspar, which has been explained by small patches of the unstable (100) surface exposed in cracks or pores.[27] Moreover, it has been shown that feldspar specimens exhibiting perthitic intergrowth are generally more ice nucleation active,[34] and that cation exchange-induced fracturing can increase the ice nucleation activity of sanidine feldspar.[32] Regarding chemical composition, K-rich feldspars are often more ice nucleation active than Na-rich feldspar,[6,8] but it is disputed whether this difference in ice nucleation activity actually comes from a higher potassium content or the prevalence of perthitic intergrowth in many K-rich feldspar.[34] The same is the case for the relation between crystallographic order in the aluminosilicate framework of K-rich feldspar minerals and their ice nucleation activity.[34,35] However, these studies are mainly limited to the micrometer and hundred-nanometre scale, while the actual ice nucleation active sites (INAS) are expected to be nanometre sized.[28,31] Consequently, the specific surface topology and chemistry of ice nucleation active sites remains elusive.

Here, we apply atomic force microscopy in ultra-high vacuum and at the solid–liquid interface to describe a micro-structure observed on microcline (001). AFM images taken under UHV conditions reveal a surface structure consisting of terraces covered by islands with a diameter between 5 nm to 40 nm, and a high density of step edges. The islands were found to exhibit the same AFM contrast as the terrace and a similar height as monolayer step edges, which suggests that the observed islands are consisting of microcline feldspar. This conclusion is supported by atomic-resolution images showing a very similar contrast and identical lattice parameters on the terrace and on the islands. Moreover, AFM images recorded at the microcline–water interface show that the observed island structure does not change noticeably within 110 min. We conclude that the investigated structure is stable in contact with water and might persist under environmental conditions. Since the presence of these feldspar islands significantly enhances the number of step and kink sites, we expect that the observed island structure—where present—might have a significant impact on surface reactivity and potentially ice nucleation activity.

2 Methods

AFM experiments were performed under ultra-high vacuum (UHV) conditions and at the solid–liquid interface. UHV AFM experiments were carried out in a UHV setup consisting of two chambers separated by a valve. The first chamber with a base pressure below 1×10^{-10} mbar was used for sample preparation and the second chamber with a base pressure below 5×10^{-11} mbar was used for AFM experiments. Dynamic AFM experiments were carried out in the frequency-modulation mode with constant amplitudes between 10 nm and 20 nm with a variable-temperature (VT) STM/AFM instrument (Scienta Omicron, Germany). The instrument was operated with a MATRIX controller. N-doped silicon cantilevers with a nominal force constant of 40 N m^{-1} and an eigenfrequency of 300 kHz (Nanosensors, Switzerland) were glued onto a cantilever holder, brought into UHV and sputter with Ar ions. To compensate for contact potentials remaining after sample preparation, a compensating voltage between 10 V and −10 V was applied.

Cuboidal microcline single crystals with the (001) direction oriented parallel to the top face and the [010] direction along one of the sample edges were obtained from SurfaceNet (Germany). X-ray diffraction data and chemical analysis confirming the sample variety as maximum microcline have been reported previously.[36,37] Samples were brought into UHV, degassed for several hours at 700 K and cleaved parallel to (001) with a tungsten carbide blade. To remove surface charges preventing AFM measurements, the samples were annealed for 20 h at 450 K.

After UHV experiments, microcline samples were locked out of the UHV chamber and clamped in a PEEK sample holder. Then, a droplet of ultrapure water (Stakpure GmbH, Germany, 18 MΩ cm) was placed on top of the sample surface before investigation with a modified[38,39] Bruker Multimode AFM with a Nanoscope V controller (Bruker Nano Surface Division, USA). Experiments were carried out with gold-coated silicon cantilevers (TAP300GD-G, Budget Sensors, Bulgaria) with a nominal force constant of 40 N m^{-1}, an eigenfrequency between 120 kHz and 140 kHz and a quality factor from 6.5 to 8.5 in water. Further in-liquid AFM measurements with a Cypher ES AFM (Asylum Research, an Oxford Instrument Company, USA) instrument were performed on microcline samples cleaved in air with a tungsten carbide blade directly before the AFM experiments. Some of the air-cleaved microcline samples were

This journal is © the Owner Societies 2025

Phys. Chem. Chem. Phys., 2025, **27**, 23574–23583 | **23575**

glued to a magnetic mounting plate with superglue, because the sample height after cleavage was not sufficient for clamping in a PEEK sample holder.

AFM images were calibrated and in case of the atomic scale images drift corrected with the drift-correction software unDrift.[40,41] Calibration parameters were determined by referencing against the known lattice parameters of calcite (10.4) in UHV and at the calcite–water interface, respectively. Scan directions are indicated in the top right corner of the images with the bold arrow pointing in the fast scan direction and the triangular arrow pointing in the slow scan direction. Surface directions indicated in the images were obtained from the manufacturers specifications and confirmed by atomic-scale imaging. The AFM channel is also marked in the top right corner with z_p being the z-piezo displacement and $\Delta\nu_{exc}$ being the excitation frequency shift.

Optical microscopy images were measured with an DCM8 optical microscope (Leica, Germany) using confocal imaging. To produce images showing the entire surface, individual images at $10\times$ magnification were stitched together. Details of the surface were inspected at $50\times$ and $150\times$ magnification. Scanning electron microscope (SEM) and energy dispersive X-ray spectroscopy (EDX) measurements were performed with a Phenom ProX G3 Desktop SEM (Thermo Fisher Scientific, USA).

3 Results and discussion

In this study, we performed AFM experiments on cleaved microcline (001) samples. Our samples are opaque white (slightly beige) microcline crystals cut from the same base crystal as the samples used in our previous studies (see UHV samples in ref. 36 and 37). Microcline is a feldspar variety with a high potassium content and a high degree of Al–Si order in the aluminosilicate framework. For our samples, both properties have previously been confirmed by chemical[37] and structural analysis.[36] Specifically, we found that our samples consist

of mainly potassium feldspar (approximately 96%) with a small amount of sodium feldspar (4%) and almost no calcium feldspar (less than 0.1%).[37] In terms of Al–Si order, our samples exhibit a high degree of aluminium–silicon order with about 80% of aluminium atoms situated in T1(o) sites.[36]

3.1 Microscopic structure

Regarding the microscopic surface structure, optical and scanning electron microscopy images reveal several micrometre big cracks and holes (see Fig. S2 and S3, ESI†). The existence of holes on both cleavage planes suggests that our microcline samples exhibit microporosity as already hypothesized in a previous study.[37] Chemical analysis of the near-surface region with SEM-EDX reveals a composition generally close to the expected composition of K-feldspar but with an increased oxygen mole fraction. We interpret this as an indication for water inclusions inside the sample, which would also be consistent with the water degassing observed in previous TPD experiments.[37] Moreover, SEM-EDX measurement reveal that our microcline samples are exsolved into K- and Na-rich domains (see Fig. S3, ESI†). Due to the observed porosity, water inclusions and exsolution structure, we expect that our samples were hydrothermally altered during their geological history.

Fig. 1(a) shows a 460×460 nm^2 AFM image taken on the (001) cleavage plane of a microcline sample prepared and analysed under UHV conditions. The image reveals a typical surface structure consisting of several terraces limited by step edges. The terraces are covered by islands, which merge with the ascending step edges of the terrace above, creating the impression of ragged step edges. To analyse the step edge height, an exemplary profile is presented in Fig. 1(b) extracted along the fast scan direction as indicated by the red line in Fig. 1(a). The extracted profile contains three step edges with an average height of (0.66 ± 0.02) nm, which is in perfect agreement with the atomic step height calculated from the bulk
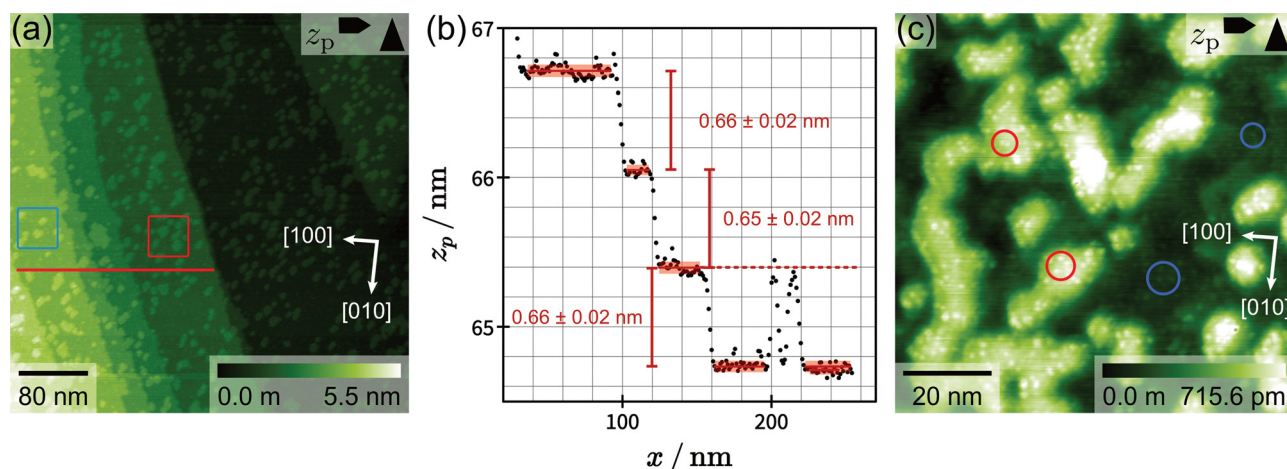

Fig. 1 (a) Experimental AFM image of the microcline (001) cleavage plane showing several step edges and islands. (b) Profile along the red line in (a) with the heights of the terraces marked. (c) Detail AFM image of the observed islands. Two examples each for the protrusions on the terrace and islands are marked by blue and red circles, respectively. AFM images are calibrated, and background corrected by means of three-point levelling. Directions indicated in the images were determined from the manufacturers specifications and confirmed with high-resolution AFM. The AFM data was recorded under UHV conditions at room temperature.

23576 | *Phys. Chem. Chem. Phys.*, 2025, **27**, 23574–23583

This journal is © the Owner Societies 2025

structure.[42] This specific image exclusively contains monoatomic step edges, but we also observed multi-step edges with heights up to several nanometres on a regular basis. However, these high step edges interfere with our high-resolution imaging, which is why areas with high step edges are typically avoided. Moreover, the step edge density on our sample varies probably due to cleavage as can be seen by comparing the micrometre scale images in, *e.g.*, Fig. 1(a) and 2(a).

Next, we turn to the islands observed on the terraces. These islands have an oval shape with irregular edges and an approximate size between 5 nm and 40 nm (largest diameter). The island coverage on the terraces is not homogeneous, some areas are almost island-free and others are densely covered. Two areas with high and low island coverage are marked by a red and blue square, respectively, in Fig. 1(a). Moreover, a 90×90 nm^2 image of the typical island structure is shown in Fig. 1(c). This image reveals that some of the islands are connected to form a larger network. The detail image also shows that both islands and terrace exhibit round protrusions with a seemingly random placement (neither the Fourier transform nor auto-correlation show any periodicity, see ESI†). These protrusions could, *e.g.*, be defects or residual surface charges. Some islands are directly attached to ascending step edges, thereby creating unusually shaped steps (see Fig. 1(a)). It is not possible to distinguish between the islands and the terrace above as both islands and terrace exhibit an identical contrast in all measured AFM channels. Furthermore, the islands have the same height as the step edges as shown by the two islands included in the extracted profile at $x \approx 200$ nm (see Fig. 1(b)). In summary, we find that the observed islands exhibit the same contrast as the terraces and a similar height as monoatomic step edges. These findings suggest that the islands are an intrinsic part of the microcline structure, and not, *e.g.*, some kind of contamination.

3.2 Atomic structure

To elucidate the atomic-scale structure of the observed islands, we measured high-resolution images on the terrace and

islands. Fig. 2(a) and (b) show an overview image of the surface and an atomic resolution image taken on the terrace in the marked area (see red rectangle in Fig. 2(a)), respectively. The atomic-resolution image reveals a periodic structure consisting of stick-like features, which we already discussed in detail in a previous publication.[36] Briefly, we found that even when prepared *in vacuo*, the as-cleaved microcline (001) surface readily reacts with even small amounts of residual water forming a hydroxylated surface.[36] In room-temperature AFM images, the hydroxyl groups closest to each other are imaged together creating the impression of stick-like features as shown in Fig. 2(b). Otherwise, microcline (001) follows the expected bulk-truncated structure without any reconstructions. A corresponding DFT model is shown in Fig. 2(c).[36] It shows the regular array of hydroxyl groups protruding from the microcline surface (hydroxyl oxygens drawn in red), where every second hydroxyl group is bound to aluminium and silicon, respectively. Our results are in perfect agreement with a recent study presenting low-temperature AFM data recorded with a copper oxide-terminated tip.[43]

AFM experiments on the islands were performed following a three-step procedure ensuring that AFM images are actually taken on an island: first, we measure an overview image (Fig. 3(a)) to find an island with a suitable size of approximately 30×30 nm^2 or bigger. Second, we choose a new scan area on top of the selected island as indicated by the red quadrangle in Fig. 3(a) and measure high-resolution images. These measurements can be challenging as we found that scanning over the islands and especially their edges increases the probability for tip changes. Here, the image measured on top of the island is presented in Fig. 3(b). It shows atomic resolution before the tip becomes unstable after approximately 60% of the image. Note that the edge in the top right corner of Fig. 3(b) nicely aligns with the sharp edge of the selected island in Fig. 3(a). Third, we increase the scan area again in Fig. 3(c) to check whether the previous measurements were indeed performed on top the island. In this regard, Fig. 3(c) shows that the scan area of the image in Fig. 3(b) (indicated by a red quadrangle) lies on
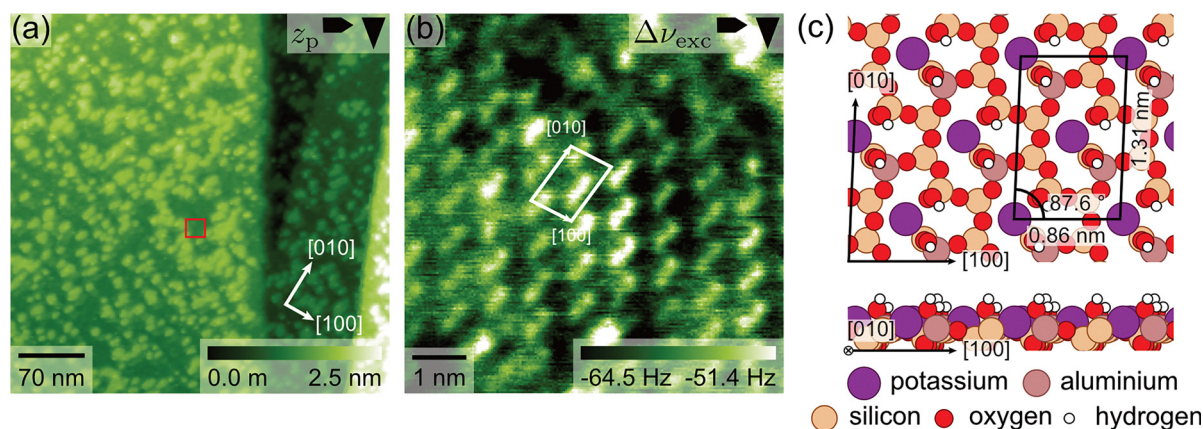

Fig. 2 Overview of the micro and atomic-scale structure on the terraces under UHV conditions. (a) Overview image of the microcline (001) surface showing the location the atomic–scale image was recorded. (b) Atomic resolution AFM image taken on the terrace in the red rectangle marked in (a). Data adapted from ref. 36. (c) Density functional theory structure of the microcline (001) surface as reported in ref. 36.
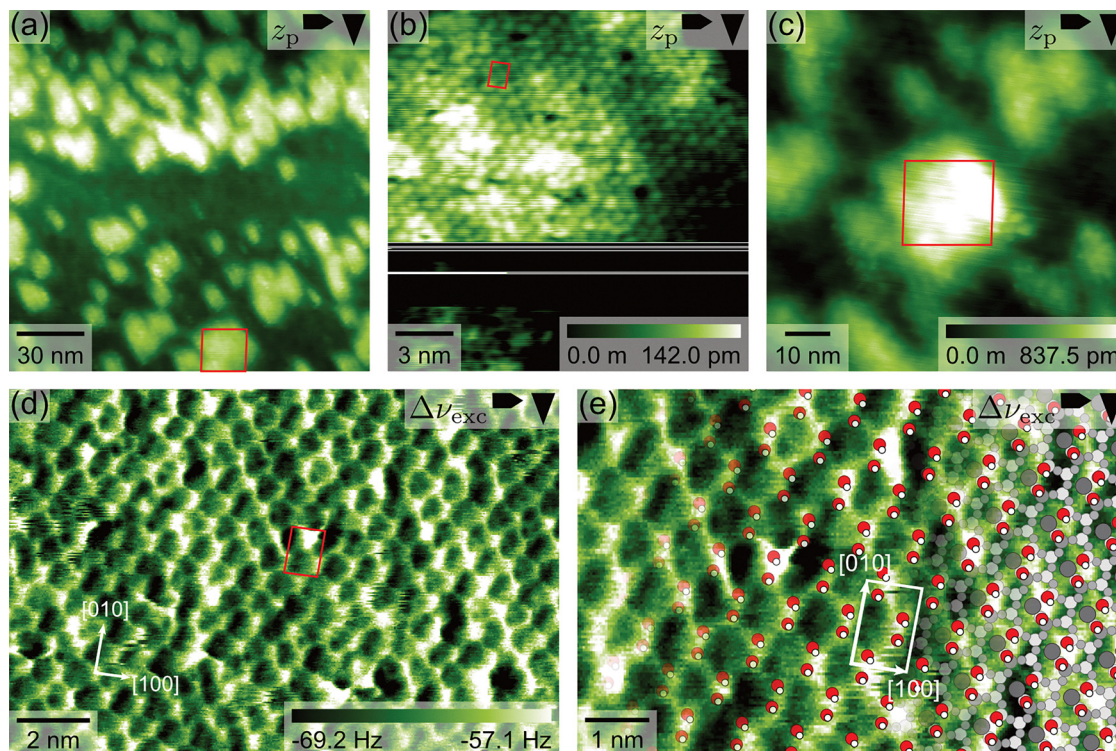
This journal is © the Owner Societies 2025

Phys. Chem. Chem. Phys., 2025, **27**, 23574–23583 | **23577**

Fig. 3 Atomic structure of the islands on microcline (001). (a)–(c) illustrate the procedure of an AFM measurement on top of an island, where (a) is an overview image, (b) is measured on top of the island and (c) is another an overview image. This procedure ensures that the measurement was indeed performed on top of an island. The scan area of (b) is indicated in (a) and (c) by red quadrangles. (d) shows an excitation frequency shift image of atomic resolution on an island (same scan area as (b)) and in (e) the DFT structure of the hydroxyl-terminated microcline surface is superimposed on the experimental AFM image. To achieve this overlay image, the experimental data was distorted with an affine transformation to match the lattice parameters of the DFT structure. The DFT structure in (e) is taken from ref. 36.

top of an island with the same shape as the island selected in the overview image Fig. 3(a). We conclude that the atomic resolution image in Fig. 3(b) was, indeed, measured on top of an island.

Based on the atomic-resolution images measured on top of the islands, we can now analyse the island structure. In the z-piezo displacement image shown in Fig. 3(b), the atomic structure consists of round protrusions arranged in a centred lattice, *i.e.*, each unit cell contains two features. On average, this lattice exhibits structural parameters of $a = (0.91 \pm 0.03)$ nm, $b = (1.29 \pm 0.02)$ nm and an angle of $\gamma = (86 \pm 3)°$ as determined from 10 AFM images. Hence, the island structure agrees with the terrace structure in all lattice parameters, and with the bulk-truncated structure in the b and γ parameters within the experimental error. Moreover, the directions of the longer (shorter) lattice vectors agree with the orientation of the [010] direction ([100] direction) of the microcline sample as specified by the manufacturer. These findings show that the structure of the islands is governed by the terrace structure underneath. Additionally, Fig. 3(b) shows some areas protruding from the surface (shown in bright white), which might correspond to the protrusions observed in the detail image Fig. 1(c). Due to the blurred appearance of these protrusions, we speculate that they might originate from surface charges remaining after the annealing.

To obtain more information on the island structure, we turn to the excitation frequency shift image shown in Fig. 3(d). In the $\Delta\nu_{exc}$ image, the island structure exhibits a different contrast consisting of bright features, which are elongated along the [010] direction. These features look similar to the sticks observed in the atomic-resolution images measured on the terrace (see Fig. 2(b)), but with a less pronounced stick-like shape. Moreover, the features on the island are connected by thinner bright lines, which creates the impression of a hexagon pattern on the surface. The great similarity between the island and terrace structures in terms of unit cell dimensions and image contrast suggests that both structures are actually identical. In this case, the difference in the atomic resolution contrast would originate from a change in the tip termination, tip-sample distance or both. This conclusion is also supported by AFM images showing atomic resolution on the terrace and small patches of an island presented in the ESI.† We further compare the atomic-structure of the islands to the DFT structure of the hydroxylated surface structure found on the terrace. In Fig. 3(e), the DFT structure from Fig. 2(b) is superimposed on a cutout of the experimental island structure. Since the focus of this overlay is on the structure within the unit cell and not the lattice parameters, we transformed the experimental image in the overlay to fit the theoretical lattice parameters. This overlay reveals a very good agreement between both

structures, where each feature is again comprised of two terminal hydroxyl groups. Moreover, we do not observe any additional surface features contradicting the superimposed structure.

3.3 Structure at the solid–liquid interface

Next we investigate the structure and stability of the discussed islands in contact with water. The microcline sample was removed from the UHV chamber, covered with a droplet of ultrapure water and inspected with AFM. Fig. 4(a) shows an AFM image taken at the microcline–water interface 27 min after bringing the sample in contact with water. In general, the island structure observed at the microcline–water interface is very similar to the topology found in UHV but with a slightly higher island density and some bigger merged islands up to around 100 nm present on the surface. However, given the inhomogeneity of the island coverage observed in the UHV experiments, we attribute this difference to the measurements taking place at a different position on the sample. The observed island structure did not change on the timescale of our experiment, $i.e.$, we did not observe dissolution or growth on the timescale of hours. The islands were observed in the first image taken at the microcline–water interface, and images taken up to 110 min after bringing the sample in contact with water show essentially the same surface topology as the first image. Additionally, we observed the reported islands on two microcline (001) surfaces prepared by cleavage under ambient conditions as shown in the ESI.† One of these surfaces was prepared by a second cleavage of the sample, which was previously used in the UHV experiments, the other sample had not been used in any experiments before.

Furthermore, we performed atomic-resolution imaging on the terrace and islands. The corresponding AFM images in Fig. 4(b) and (c) show a periodic structure with two round features per unit cell and an identical image contrast in both cases. This image contrast is identical to the contrast reported on another microcline (001) sample in our previous publication, which is why we can assign it to imaging in the second

water layer on the surface.[36] The lattice parameters observed on the terrace ($a = (0.88 \pm 0.03)$ nm, $b = (1.29 \pm 0.03)$ nm and $\gamma = (85 \pm 2)°$) and islands ($a = (0.85 \pm 0.03)$ nm, $b = (1.32 \pm 0.03)$ nm and $\gamma = (86 \pm 2)°$) are also identical within the accuracy of our device.[40] These findings, again, indicate that the observed islands have a very similar structure than the microcline surface underneath.

3.4 Origin of islands

In the previous sections, we established that the observed islands have the same height as atomic step edges on microcline (001) and that the atomic structures in UHV and at the solid–liquid interface closely resemble bare microcline (001). Further, we found that the islands are stable in contact with water on the timescale of hours. Based on these results, we will now discuss three possible explanations for the observed island structure. The islands could originate from (1) a contamination introduced during sample preparation, (2) alteration of the surface structure by sample preparation and (3) internal microstructure exposed upon cleavage. It is essential to understand the origin of the islands, because a surface structure induced by contamination or sample preparation might not be relevant in a geochemical context. In contrast, the observed islands could have important implication for processes on feldspar minerals, if they can form on natural feldspar samples under environmental conditions.

First, we discuss whether the islands could be caused by contaminations. For example, the annealing of our samples could release (organic) molecules, which then adsorb on the cleaved microcline (001) surface and form islands. Island formation by (organic) adsorbates has been observed both under UHV conditions[44–46] and at the mineral–water interface,[47–49] and the periodicity on these islands often follows the lattice of the mineral surface underneath. The internal structure of adsorbate islands typically differs from the mineral substrate.[44–49] Here, however, we observe an extremely similar atomic structure on the terrace and islands. Moreover, the observed islands are very
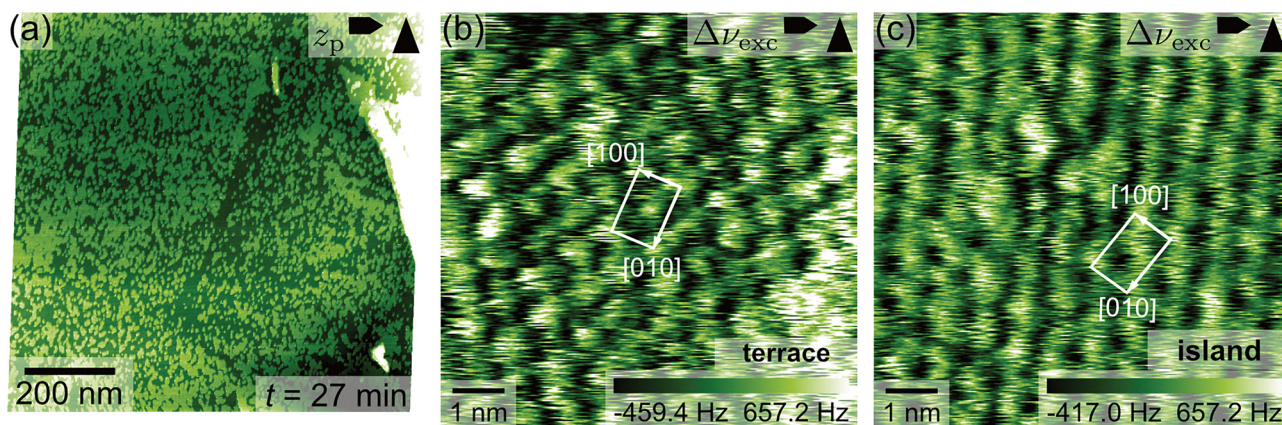

Fig. 4 AFM images taken at the microcline (001)–water interface showing that the observed island structure persists in contact with water. (a) shows a typical 2.0×2.0 μm² overview image measured 27 min after the water droplet was placed on the sample. Atomic-resolution images measured on the terrace and island are shown in (b) and (c). The AFM contrast and lattice parameters in (b) and (c) are identical, further corroborating the intrinsic nature of the observed feldspar islands.

homogeneous in their height, internal structure and general appearance, which is contrary to our expectation for contaminated samples. In case of contaminations, we expect a very diverse surface structure caused by a variety of contaminants.[50,51] Further, we not only observed islands for samples prepared in UHV, but also for samples cleaved in ambient conditions and analysed at the mineral–water interface (see ESI†). It seems very unlikely to observe the same contamination after these completely different methods of sample preparation. Moreover, SEM-EDX analysis of two of our samples with islands showed no signs of organic contamination as discussed in the ESI.† Consequently, we exclude contaminations as a potential origin for the observed islands.

Second, we explore a potential alteration of the surface structure during sample preparation. Prior to our UHV-AFM experiments, we needed to anneal our samples for several hours to remove surface charges induced by cleavage, so the observed islands might also have formed during this annealing step. To test this hypothesis, we freshly cleaved a microcline sample from the same batch under ambient conditions and annealed it to subsequently higher temperatures (449 K, 549 K and 649 K). Directly after cleavage and after each annealing step, we inspected the surface with AFM at the microcline–water interface, which allowed us to assess the surface topology regardless of surface charges. As shown in the ESI,† this sample did not exhibit any islands initially, and we could not induce the formation of islands by annealing up to 649 K for 20 h. These annealing experiments suggest that the observed structure is likely not caused by annealing, which is consistent with the fact that we also observed islands on air-cleaved samples (see ESI†).

Moreover, the microcline samples could be altered upon contact with water. In the UHV experiments, the water can originate from the sample by degassing during annealing as reported previously.[37] In the liquid experiments, the surface can react with the water droplet placed on top of the sample. Indeed, literature shows that K-feldspar can be altered through hydrolysis in water or acidic solution, leading to the formation of phyllosilicate minerals, silicic acid and potassium hydroxide.[52] The first step in K-feldspar weathering is likely the leaching of potassium ions from the first interfacial layers, which is followed by protonation of the aluminosilicate framework.[16,52] This process is expected to preferentially occur along fractures inside the K-feldspar minerals.[52] These weathering schemes suggest either the formation of a potassium-depleted aluminosilicate layer or the formation of a hydrolysed aluminosilicate (clay-like) layer. However, if water was altering the feldspar terrace, we should not observe islands but patches of altered surface layer or even holes in the surface, while islands are indicative of reprecipitation. Furthermore, since we observe an island structure, which is indistinguishable from the bare feldspar surface, we must assume that feldspar material from the solution reprecipitates as islands on the terrace. The material likely stems from dissolution *via* hydrolysis at fracture sites, cracks or at the phase boundary between K- and Na-rich domains, the presence of which is clearly revealed by optical and scanning electron microscopy (see ESI†).

Nevertheless, the question remains why feldspar material reprecipitates as roundish islands instead of forming closed layers. For gibbsite precipitating on muscovite mica (001), it has been found that gibbsite forms islands approximately 10 nm in lateral extent and a single monolayer thick, separated by 1 nm to 2 nm spaces instead of a complete gibbsite layer.[49] One of several explanations offered for this peculiar observation has been electrostatic repulsion between atoms at the edges of islands, which might prevent coalescence and therefore limits island size.[49] In our case, it seems unlikely that the observed island distribution is caused by electrostatic repulsion between islands, because the island density varies significantly with some of the islands being several nanometres away from each other. Instead, the varying island density seems to suggest that we are looking at different stages of island growth.

Further, the dissolution rates of K-feldspar derived from experiments with feldspar powder indicate a process on the timescale of hours or slower,[16] which is significantly slower than our AFM experiments. While the surface alteration process might have already started between placement of the water droplet and the first AFM image taken at the microcline–water interface, we would expect to see a further surface alteration during our AFM experiments. The fact that we do not observe any alteration to the surface structure, thus, contradicts the hypothesis of K-feldspar weathering during sample preparation.

Third, the observed islands could originate from a structure already contained within the microcline samples, which is exposed upon cleavage. Our microcline samples are exsolved into K- and Na-rich domains and their turbid appearance also suggests that the samples have undergone hydrothermal alteration. As discussed in the introduction, exsolved and weathered K-feldspar samples commonly exhibit complex microstructure,[18–25] which could be exposed upon cleavage. However, for a structure originating from cleavage we would expect to observe two distinct properties: the cleavage should create both islands and holes, and the two sides of the cleavage plane should exhibit an opposite pattern. The islands on microcline (001) satisfy neither of these expectations, because we exclusively observed islands and experiments on an air-cleaved microcline sample revealed islands on both cleavage planes (see ESI†). This makes it very unlikely that the islands are created by cleavage of bulk microstructure.

Cleavage could not only expose bulk microstructure, but also structures previously hidden on internal surfaces of the microcline samples. As shown in Fig. S1 (ESI†), our microcline samples exhibit several natural cracks parallel to the (001) cleavage plane, and we observed that samples tend to cleave along these cracks even if scored slightly above or below. Consequently, at least some of the surfaces investigated in our experiments will be old surfaces created by the cracking rather than our cleavage. In this case, the islands could have formed naturally on the inside of cracks by one of the previously discussed chemical alteration schemes over a longer timescale before they are exposed by the cleavage. This hypothesis is consistent with the observation of islands on both cleavage planes and the fact that we do not observe any further

23580 | *Phys. Chem. Chem. Phys.*, 2025, **27**, 23574–23583

This journal is © the Owner Societies 2025

surface alteration in our experiments at the mineral–water interface. Moreover, the surface alteration could have processed with different speeds in different areas of the cracks, which would explain the widely different island densities observed in our experiments. However, in this scenario we would also expect areas without islands originating from the cleavage in areas without cracks, but this has only been observed very rarely.

The hypothesis of the islands having previously formed in cracks and being exposed upon cleavage is also consistent with the statistics of our AFM experiments on microcline (001). We investigated a total of seven cleavage planes from the batch of opaque white to beige microcline samples, of which four showed the discussed island structure. This seems reasonable, because our samples might not always cleave along cracks and the degree of chemical alteration might vary locally even in the same base crystal. In a previous publication,[36] we also investigated transparent colourless microcline samples without apparent internal cracks. On these samples, we never observed any island structure as might have been expected from the absence of obvious internal cracks and signs of significant chemical alteration.

Based on this discussion, we think that island formation inside of cracks during previous weathering and exposure by cleavage is the most likely explanation for the experimental results. In this case, the observed islands would be a natural feature of the microcline (001) surface, which could not only appear on feldspar surfaces in rocks but also on the surface of feldspar mineral dust particles.

4 Conclusions

In summary, we present high-resolution AFM images of K-feldspar microcline (001) taken under UHV conditions and at the mineral–water interface. Micrometre-scale images reveal a surface consisting of terraces covered by islands with a size from 5 nm to around 100 nm. The islands have the same height as monolayer step edges and exhibit the same contrast as the terrace in all AFM channels, indicating that the islands are an intrinsic part of the feldspar crystal. This finding is corroborated by atomic-resolution images on the terrace and on top of the islands showing the same atomic-scale structure in both UHV experiments and at the mineral–water interface. As an intrinsic surface feature, these islands significantly increase the number of kink and edge sites on the surface compared to a surface with flat terraces. Furthermore, we find that the surface topology does not change when in contact with liquid water on the timescale of our experiments which extends to 110 min. We conclude that the observed island structure is stable in contact with water, which indicates that it might persist under environmental conditions. Given the known importance of step and kink sites for dissolution, growth and general surface reactivity of minerals, we expect that the presence or absence of these island structures can significantly alter processes on feldspar samples. This, in turn, might have important implications for understanding reactivity and processes on feldspar minerals.

Author contributions

Conflicts of interest

There are no conflicts to declare.

Data availability

The data supporting this article have been included as part of the ESI.†

Acknowledgements

Notes and references

1 W. A. Deer, R. A. Howie and J. Zussman, *An introduction to the rock-forming minerals*, Mineralogical Society of Great Britain and Ireland, 2013.
2 R. A. Berner, A. C. Lasaga and R. M. Garrels, *Am. J. Sci.*, 1983, **283**, 641–683.
3 J. Hartmann, A. J. West, P. Renforth, P. Köhler, C. L. De La Rocha, D. A. Wolf-Gladrow, H. H. Dürr and J. Scheffran, *Rev. Geophys.*, 2013, **51**, 113–149.
4 C. G. Ramos, J. C. Hower, E. Blanco, M. L. S. Oliveira and S. H. Theodoro, *Geosci. Front.*, 2022, **13**, 101185.
5 B. J. Murray, D. O'Sullivan, J. D. Atkinson and M. E. Webb, *Chem. Soc. Rev.*, 2012, **41**, 6519–6554.
6 J. D. Atkinson, B. J. Murray, M. T. Woodhouse, T. F. Whale, K. J. Baustian, K. S. Carslaw, S. Dobbie, D. OSullivan and T. L. Malkin, *Nature*, 2013, **498**, 355–358.
7 J. D. Yakobi-Hancock, L. A. Ladino and J. P. D. Abbatt, *Atmos. Chem. Phys.*, 2013, **13**, 11175–11185.
8 A. D. Harrison, T. F. Whale, M. A. Carpenter, M. A. Holden, L. Neve, D. O'Sullivan, J. Vergara Temprado and B. J. Murray, *Atmos. Chem. Phys.*, 2016, **16**, 10927–10940.
9 C. Hoose and O. Möhler, *Atmos. Chem. Phys.*, 2012, **12**, 9817–9854.
10 M. B. Baker, *Science*, 1997, **276**, 1072–1078.
11 P. A. Arias, N. Bellouin, E. Coppola, R. G. Jones, G. Krinner, J. Marotzke, V. Naik, M. D. Palmer, G.-K. Plattner, J. Rogelj, M. Rojas, J. Sillmann, T. Storelvmo, P. W. Thorne, B. Trewin, K. Achuta Rao, B. Adhikary, R. P. Allan, K. Armour, G. Bala,

This journal is © the Owner Societies 2025

Phys. Chem. Chem. Phys., 2025, **27**, 23574–23583 | **23581**

S. Barimalala, S. Berger, J. G. Canadell, A. Cassou, A. Cherchi, W. Collins, D. S. Collins, S. Connors, S. Corti, F. Cruz, F. J. Dentener, A. Dereczynski, A. Di Luca, F. Diongue Niang, F. J. Doblas-Reyes, A. Dosio, H. Douville, F. Engelbrecht, V. Eyring, E. Fischer, P. Forster, B. Fox-Kemper, J. S. Fuglestvedt, J. C. Fyfe, N. P. Gillett, L. Goldfarb, J. M. Gorodetskaya, R. Gutierrez, R. Hamdi, E. Hawkins, H. T. Hewitt, A. Hope, S. Islam, C. Jones, R. E. Kaufman, Y. Kopp, J. Kosaka, J. Kossin, S. Krakovska, J. Lee, T. Li, T. K. Mauritsen, A. M. Maycock, S.-K. Meinshausen, D. P. Min, P. M. S. Monteiro, F. Ngo-Duc, I. Otto, A. Pinto, K. Pirani, R. Raghavan, A. C. Ranasinghe, A. C. Ruane, L. Ruiz, B. H. Sallée, B. H. Samset, S. I. Sathyendranath, A. A. Seneviratne, A. Sörensson, I. Szopa, Y. Takayabu, A.-M. Tréguier, B. van den Hurk, R. Vautard, K. von Schuckmann, S. Zaehle, X. Zhang and K. Zickfeld, in *Climate change 2021: The physical science basis. Contribution of working group I to the sixth assessment report of the intergovernmental panel on climate change*, ed. V. Masson-Delmotte, A. P. P. Zhai, C. P. S. L. Connors, N. C. S. Berger, L. G. Y. Chen, M. H. M. I. Gomis, E. L. K. Leitzell, T. K. M. J. B. R. Matthews, O. Y. T. Waterfield, R. Yu and B. Zhou, Cambridge University Press, 2021, ch. Technical Summary, pp. 35–144.

12 A. J. Gratz, P. E. Hillner and P. K. Hansma, *Geochim. Cosmochim. Acta*, 1993, **57**, 491–495.

13 Y. Liang, D. R. Baer, J. M. McCoy, J. E. Amonette and J. P. Lafemina, *Geochim. Cosmochim. Acta*, 1996, **60**, 4883–4887.

14 Y. Liang and D. R. Baer, *Surf. Sci.*, 1997, **373**, 275–287.

15 I. Parsons, J. D. Fitz Gerald and M. R. Lee, *Am. Mineral.*, 2015, **100**, 1277–1303.

16 *Feldspars and their reactions*, ed. I. Parsons, Springer, Netherlands, 1994, p. 650.

17 M. Okrusch and S. Matthes, *Mineralogie*, Springer, Berlin Heidelberg, 2014.

18 R. Abart, E. Petrishcheva, R. Wirth and D. Rhede, *Am. J. Sci.*, 2009, **309**, 450–475.

19 C. Evangelakakis, H. Kroll, G. Voll, H.-R. Wenk, H. Meisheng and J. Köpcke, *Contrib. Mineral. Petrol.*, 1993, **114**, 519–532.

20 I. Parsons, J. D. Fitz Gerald, J. K. W. Lee, T. Ivanic and U. Golla-Schindler, *Contrib. Mineral. Petrol.*, 2010, **160**, 155–180.

21 W. L. Brown and I. Parsons, *Contrib. Mineral. Petrol.*, 1984, **86**, 335–341.

22 I. Parsons, J. D. Fitz Gerald, M. T. Heizler, L. L. Heizler, T. Ivanic and M. R. Lee, *Contrib. Mineral. Petrol.*, 2013, **165**, 931–960.

23 M. R. Lee, K. A. Waldron and I. Parsons, *Mineral. Mag.*, 1995, **59**, 63–78.

24 J. D. Fitz Gerald, I. Parsons and N. Cayzer, *Am. Mineral.*, 2006, **91**, 772–783.

25 R. H. Worden, F. D. L. Walker, I. Parsons and W. L. Brown, *Contrib. Mineral. Petrol.*, 1990, **104**, 507–515.

26 M. R. Lee, K. A. Waldron, I. Parsons and W. L. Brown, *Contrib. Mineral. Petrol.*, 1997, **127**, 291–304.

27 A. Kiselev, F. Bachmann, P. Pedevilla, S. J. Cox, A. Michaelides, D. Gerthsen and T. Leisner, *Science*, 2017, **355**, 367–371.

28 M. A. Holden, T. F. Whale, M. D. Tarn, D. OSullivan, R. D. Walshaw, B. J. Murray, F. C. Meldrum and H. K. Christenson, *Sci. Adv.*, 2019, **5**, eaav4316.

29 M. A. Holden, J. M. Campbell, F. C. Meldrum, B. J. Murray and H. K. Christenson, *Proc. Natl. Acad. Sci. U. S. A.*, 2021, **118**, e2022859118.

30 R. W. Friddle and K. Thürmer, *Nanoscale*, 2019, **11**, 21147–21154.

31 E. Pach and A. Verdaguer, *J. Phys. Chem. C*, 2019, **123**, 20998–21004.

32 A. A. Kiselev, A. Keinert, T. Gaedeke, T. Leisner, C. Sutter, E. Petrishcheva and R. Abart, *Atmos. Chem. Phys.*, 2021, **21**, 11801–11814.

33 A. Keinert, K. Deck, T. Gaedeke, T. Leisner and A. A. Kiselev, *Faraday Discuss.*, 2022, **235**, 148–161.

34 T. F. Whale, M. A. Holden, A. N. Kulak, Y.-Y. Kim, F. C. Meldrum, H. K. Christenson and B. J. Murray, *Phys. Chem. Chem. Phys.*, 2017, **19**, 31186–31193.

35 A. Welti, U. Lohmann and Z. A. Kanji, *Atmos. Chem. Phys.*, 2019, **19**, 10901–10918.

36 T. Dickbreder, F. Sabath, B. Reischl, R. V. E. Nilsson, A. S. Foster, R. Bechstein and A. Kühnle, *Nanoscale*, 2024, **16**, 3462–3473.

37 T. Dickbreder, F. Schneider, L. Klausfering, K. N. Dreier, F. Sabath, A. S. Foster, R. Bechstein and A. Kühnle, *Phys. Chem. Chem. Phys.*, 2025, DOI: **10.1039/d5cp01796c**.

38 H. Adam, S. Rode, M. Schreiber, K. Kobayashi, H. Yamada and A. Kühnle, *Rev. Sci. Instrum.*, 2014, **85**, 023703.

39 S. Rode, R. Stark, J. Lübbe, L. Tröger, J. Schütte, K. Umeda, K. Kobayashi, H. Yamada and A. Kühnle, *Rev. Sci. Instrum.*, 2011, **82**, 073703.

40 T. Dickbreder, F. Sabath, L. Höltkemeier, R. Bechstein and A. Kühnle, *Beilstein J. Nanotechnol.*, 2023, **14**, 1225–1237.

41 T. Dickbreder and F. Sabath, unDrift v1.0 – SPM image drift correction and calibration, 2023, **https://pc1.pages.ub.uni-bielefeld.de/pub/2023-unDrift-1.0/unDrift/index.html**.

42 S. W. Bailey, *Am. Mineral.*, 1969, **54**, 1540–1545.

43 G. Franceschi, A. Conti, L. Lezuo, R. Abart, F. Mittendorfer, M. Schmid and U. Diebold, *J. Phys. Chem. Lett.*, 2023, **15**, 15–22.

44 F. Schneider, L. Höltkemeier, A. Floris, L. Kantorovich, R. Bechstein and A. Kühnle, *Phys. Chem. Chem. Phys.*, 2024, 12282–12288.

45 T. Dienel, C. Loppacher, S. C. B. Mannsfeld, R. Forker and T. Fritz, *Adv. Mater.*, 2008, **20**, 959–963.

46 P. Rahe, M. Nimmrich and A. Kühnle, *Small*, 2012, **8**, 2969–2977.

47 M. Nalbach, P. Raiteri, S. Klassen, S. Schäfer, J. D. Gale, R. Bechstein and A. Kühnle, *J. Phys. Chem. C*, 2017, **121**, 24144–24151.

48 W. Foster, J. A. Aguilar, H. Kusumaatmaja and K. Voïtchovsky, *ACS Appl. Mater. Interfaces*, 2018, **10**, 34265–34271.

23582 | *Phys. Chem. Chem. Phys.*, 2025, **27**, 23574–23583

This journal is © the Owner Societies 2025

49 J. E. Stubbs, B. A. Legg, S. S. Lee, P. Dera, J. J. De Yoreo, P. Fenter and P. J. Eng, *J. Phys. Chem. C*, 2019, **123**, 27615–27627.

50 F. Ostendorf, C. Schmitz, S. Hirth, A. Kühnle, J. J. Kolodziej and M. Reichling, *Nanotechnology*, 2008, **19**, 305705.

51 S. Seibert, S. Klassen, A. Latus, R. Bechstein and A. Kühnle, *Langmuir*, 2020, **36**, 7789–7794.

52 W. Bland and D. Rolls, in *Weathering*, ed. Arnold, London, 1998.

This journal is © the Owner Societies 2025

Phys. Chem. Chem. Phys., 2025, **27**, 23574–23583 | **23583**